Ocean Engineering 334 (2025) 121554

Contents lists available at ScienceDirect

Ocean Engineering

journal homepage: www.elsevier.com/locate/oceaneng

Research paper

Experimental investigation of hydroelastic response and resonance characteristics in anaconda wave energy converter

Yang Huang [a], Qing Xiao [a,*], Saishuai Dai [a], Lin Cui [b], Liu Yang [c], Saeid Lotfian [a], Farhad Abad [a], Guillermo Idarraga [c], Feargal Brennan [a]

[a] Department of Naval Architecture, Ocean & Marine Engineering, University of Strathclyde, Glasgow, G4 0LZ, UK
[b] Marine Technology Innovation Centre Yangtze Delta, Jiangshu 212003, China
[c] Advanced Composite Group, Department of Mechanical and Aerospace Engineering, University of Strathclyde, Glasgow, G1 1XJ, UK

ARTICLE INFO

Keywords:
Anaconda wave energy converter
Flexible material
Wave tank test
Hydroelastic responses
Resonant responses

ABSTRACT

The Anaconda wave energy converter (WEC) is a novel category within flexible material WECs. Its simple structural design, ease of transportation and installation, and adaptability to diverse sea conditions have attracted significant attention. Although previous studies have included several wave tank experiments and numerical analyses on the Anaconda WEC, a systematic investigation of its hydroelatic response under different configurations is still lacking. To address this gap, a series of wave tank tests were conducted at the Kelvin Hydrodynamics Laboratory in the United Kingdom using five scaled physical models with variations in tube geometry, material properties, excess pressure, and power take-off (PTO) damping. Measurements of tube deformation and PTO response were employed to evaluate the device's hydroelastic performance. The results reveal that resonance occurs not only when the external water wave phase speed aligns with the free bulge wave speed inside tube, but also at the natural frequencies associated to the tube's heave and surge motions, as well as the PTO dynamics. Tube stiffness, geometry, and excess pressure emerged as critical factors influencing these resonant conditions, while increases in PTO damping and wave amplitude further amplified the response and energy capture. Moreover, the spatial deformation of the tube displayed distinct modal patterns under different resonant conditions. These findings provide essential insights into the hydroelastic behaviour of flexible WECs, laying a robust foundation for optimizing design and validating future numerical models.

1. Introduction

The increasing global demand for renewable energy has driven extensive research into ocean wave energy, a vast and largely untapped resource. Among the various available technologies, wave energy converters (WECs) have emerged as promising candidates for sustainable energy production (Guo and Ringwood, 2021; Mwasilu and Jung, 2019; Ang et al., 2022). Traditional WECs typically rely on one or more interconnected rigid bodies as primary wave absorbers. However, due to their rigidity, these structures experience significant forces and stress concentrations under real sea conditions, making them more susceptible to structural damage. This, in turn, increases operation and maintenance costs and ultimately raises the overall cost of energy production (Aderinto and Li, 2018; Falcão, 2010; Uihlein and Magagna, 2016).

To address these limitations, flexible WECs have been proposed, incorporating flexible components as the primary wave absorbers and/or within the power take-off (PTO) system (Collins et al., 2021; Moretti et al., 2020). The inherent compliance of flexible structures enables a more uniform stress distribution, mitigating fatigue damage and enhancing long-term reliability. Additionally, their lightweight nature reduces material costs and facilitates transportation and installation. Their ability to deform under extreme wave conditions improves survivability, minimizes structural damage, and ultimately lowers maintenance costs while extending operational lifespan (Jean et al., 2012).

A representative example of a flexible WEC is the Anaconda WEC (Farley and Rainey, 2011; Farley et al., 2012), as shown in Fig. 1. It consists of a water-filled horizontal elastic tube floating just beneath the sea surface and a PTO system. Due to its fully submerged, compliant, and streamlined design, the device can avoid direct wave impacts and adapt to varying sea states through its inherent flexibility. These features contribute to reduced structural loading and enhanced durability under extreme environmental conditions. Moreover, the survivability of the

* Corresponding author.
E-mail address: qing.xiao@strath.ac.uk (Q. Xiao).

https://doi.org/10.1016/j.oceaneng.2025.121554
Received 11 March 2025; Received in revised form 25 April 2025; Accepted 12 May 2025
Available online 23 May 2025

system can be further improved by increasing the ballast water, allowing the device to submerge deeper and stay farther from the free surface during harsh sea states.

The working principle of the Anaconda WEC can be briefly described as follows: As ocean waves propagate over the device, they exert a time-varying pressure on the tube walls, causing periodic expansion and contraction of the tube structure. This wave-induced deformation, driven by fluid pressure fluctuations within the flexible tube, generates a bulge wave, a traveling wave that propagates along the tube's axis. This mechanism converts wave energy into the kinetic energy of the internal fluid, enabling efficient energy transfer within the system. To convert this harvested energy into useful electricity, the device employs a hydraulic PTO system. The bulge wave-induced fluid motion is directed toward the stern of the tube, where it passes through a set of hydraulic valves and accumulators. These components absorb flow fluctuations and store pressure energy, which is subsequently used to drive hydraulic turbines that generate electricity. The hydraulic PTO's ability to efficiently extract energy from oscillatory internal flow, while maintaining compactness and durability in harsh marine environments, makes it a good choice for such flexible, enclosed systems.

Several experimental and numerical studies have been conducted on the Anaconda WEC. Chaplin et al., 2007a, 2007b performed the first wave tank test on a small-scale 2.5 m-long Anaconda WEC, demonstrating significant capture width over a range of incident wave frequencies. Heller et al. (2010) later conducted a series of experiments on a 1:25 scale model (a 7 m-long rubber tube) at the Danish Hydraulic Institute, finding that the capture width is maximized when the free bulge wave speed matches the external water wave phase speed. Subsequently, Chaplin et al. (2012) and Farley et al. (2012) carried out additional experiments using the same 1:25 scale model in the towing tank at Southampton Solent University. These tests, employing a linear pneumatic PTO with adjustable impedance, provided insights into the effect of PTO impedance on the WEC's efficiency. Concurrently, a reduced-order numerical model based on potential flow theory and tube distensibility equations was developed, showing good agreement with experimental bulge wave behaviour. However, it is important to note that these reduced-order models assume the tube remains fully submerged, which may not accurately reflect real operating conditions. Additionally, in these experiments, both ends of the Anaconda WEC were fixed, a constraint that deviates from actual deployment scenarios.

Further investigations were conducted by Mendes et al. (2014), who tested a 1:100 scale Anaconda WEC equipped with a nonlinear pneumatic PTO system (an orifice plate). In these experiments, the bow was connected to an anchor chain, allowing the Anaconda WEC to float freely, while its stern was fixed. These tests examined power output and energy capture efficiency across varying PTO damping conditions in deep and intermediate regular waves. Mendes et al. (2017) also conducted additional wave tank tests on a 1:50 scale model, focusing on the impact of air compressibility of the pneumatic PTO on power output and assessing scale-dependent performance variations. Furthermore, Yu et al. (2024) investigated the influence of relative hydraulic head of the pneumatic PTO on the WEC's hydrodynamic efficiency using a 4 m-long model.

Despite the above valuable experimental studies, previous research has primarily focused on the working mechanism of the Anaconda WEC and the influence of PTO damping on its efficiency. However, there remains a lack of systematic investigation into the effects of tube geometry (length, diameter, thickness), material properties, wave conditions, excess pressure, and PTO damping on the hydroelastic response of the Anaconda WEC.

To address this gap, this study presents a series of towing tank experiments conducted at the Kelvin Hydrodynamics Laboratory (KHL), University of Strathclyde (Kelvin Hydrodynamics Laboratory, 2025), investigating the performance of the Anaconda WEC under varying tube geometries, material properties, internal excess pressures, PTO damping levels, and wave amplitudes. The experimental data are analysed to assess the influence of these parameters on the device's hydroelastic response and power output.

This work aims not only to deepen the understanding of the fluid-structure interaction (FSI) mechanisms governing the Anaconda WEC, particularly its resonance behaviour, but also to generate a high-quality dataset for future model development. The resulting data are expected to serve as a benchmark for validating numerical hydroelastic models and to support the design, optimization, and eventual real-world deployment of flexible wave energy converters.

The remainder of this paper is structured as follows: Section 2 describes the experimental setup, including the wave tank facilities, WEC model design, measurement techniques, and data processing methods. Section 3 details the material characterization of different flexible materials. Section 4 presents and discusses the experimental results, with a focus on resonance responses and the effects of key design parameters. Finally, Section 5 summarizes the main findings and outlines directions for future research.

2. Experimental overview

2.1. Wave tank

In this study, all wave tank tests for the Anaconda model were conducted in the towing tank at the KHL, University of Strathclyde. The tank, measuring 76 m in length, 4.6 m in width, and 2.0 m in water depth, is equipped with a four-flap active absorbing wavemaker capable of generating regular waves exceeding 0.6 m and irregular waves over 0.75 m in height. A 14 m-long passive slope type beach, installed at the wavemaker's opposite end, facilitates wave absorption and offers a maximum wave reflection coefficient less than 5 % within the interested wave frequencies. Fig. 2 illustrates the main features of the towing tank.

2.2. Physical model

The experimental Anaconda model and its primary configuration are adopted from the work of Mendes et al., 2014, 2017, with notable modifications in geometric dimensions, materials, and experimental setup. As illustrated in Fig. 3, the primary mover of the Anaconda model is a slender, flexible tube filled with pressurized water. The tube bow features a bullet-shaped structure that exhibits natural buoyancy and is connected to a fixed anchorage point via a horizontally positioned mooring line. In the experiments, an elastic rope served as the mooring.

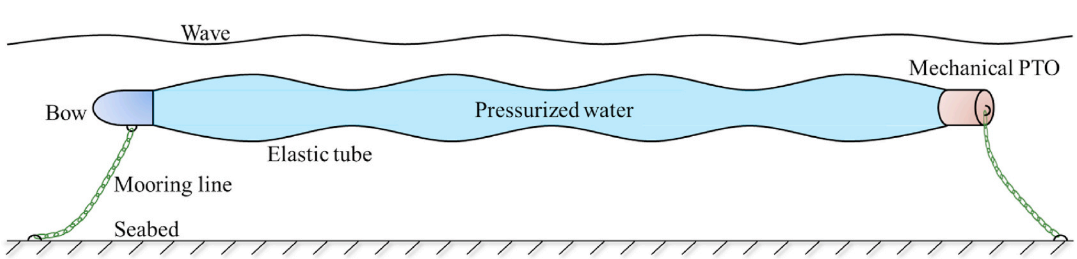

Fig. 1. Schematic diagram of the Anaconda WEC.

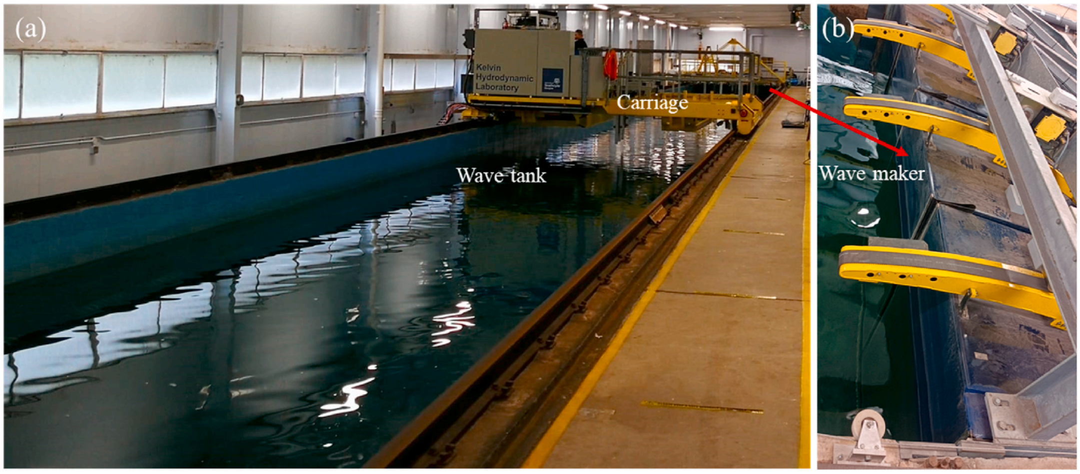

Fig. 2. Photos of (a) KHL wave tank; (b) wave maker.

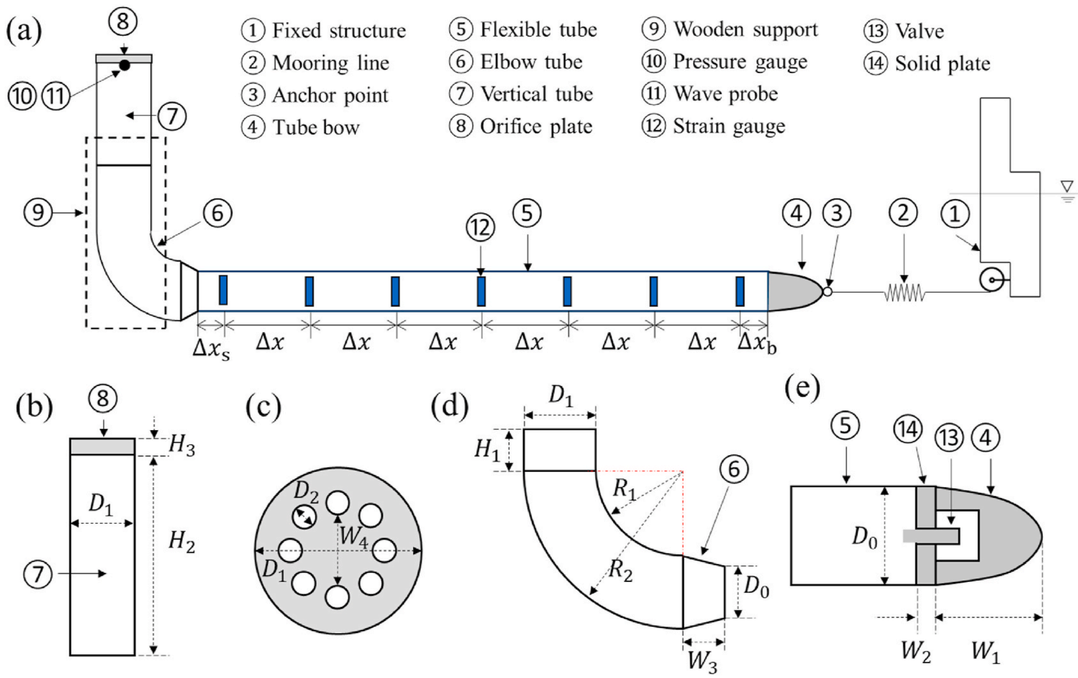

Fig. 3. Schematic diagram of the Anaconda WEC model: (a) overview of Anaconda model; (b) vertical tube; (c) orifice plate; (d) elbow tube; (e) tube bow.

The tube's tail is attached to an elbow tube, which is further connected to a vertical PVC tube capped by an orifice plate. This orifice plate acts as a simplified surrogate for the PTO system in the experimental setup. In a real Anaconda WEC, the PTO typically consists of a hydraulic system comprising valves, accumulators, and hydraulic turbines. The adoption of an orifice plate in this study, following previous experimental practices (Mendes et al., 2014, 2017), is intended to provide a practical and simplified means of emulating the energy dissipation behaviour of the actual PTO. Table 1 presents the main dimensions of all components of the Anaconda model, excluding the flexible tube.

To investigate the influence of the flexible tube's geometrical dimensions, including tube length, wall thickness, and diameter, on the hydroelastic responses of the Anaconda WEC, five flexible tubes with varying geometrical parameters were tested. The detailed dimensions of these tubes are summarized in Table 2. Additionally, two different materials, NR45 (natural rubber with a 45° shore hardness) and NR70 (natural rubber with a 70° shore hardness), were examined to assess the impact of material properties on the WEC. It is worth mentioning that

Table 1
Geometry dimensions of the Anaconda model (Unit: mm).

Component	Symbol	Meaning	Value
Vertical tube	D_1	Diameter of the vertical tube	300
	H_2	Height of vertical tube	1400
	H_3	Thickness of the orifice plate	50
Orifice plate	D_2	Diameter of hole on orifical plate	42
	W_3	Distance between holes	172
Elbow tube	R_1	Inner radius of elbow tube	100
	R_2	Outer radius of elbow tube	400
	W_3	Length of the horizontal transition tube	100
	H_1	Length of the vertical transition tube	50
Nose	W_1	Length of the nose	430
	W_2	Thickness of the solid plate	50

Table 2
Material and geometrical parameters of flexible tubes.

No.	Length L_t	Diameter D_0	Thickness t_0	Material
Tube 1	2.8 m	165 mm	2.6 mm	NR45
Tube 2	6.7 m	165 mm	2.2 mm	NR45
Tube 3	6.8 m	165 mm	3.5 mm	NR45
Tube 4	5.0 m	200 mm	1.5 mm	NR70
Tube 5	5.0 m	200 mm	3.0 mm	NR45

although Tubes 1–3 and Tube 5 are all made from NR45, their material properties may vary due to differences between production batches. The stress-strain behaviours of these tubes are described in the subsequent section.

It is notable that the parameters of the five flexible tubes do not strictly adhere to the single-variable principle. This is attributable to several factors. On one hand, manufacturing a long, large-diameter, uniform thickness, and thin flexible tube is inherently challenging. The tubes employed in this study are obtained through a combination of customization by Checkmate Flexible Engineering Ltd. (Checkmate Flexible Engineering Ltd, 2025) and borrowing tubes from previous experiments. Consequently, due to manufacturing constraints and the limited availability of tubes, it is not feasible to ensure that any two tubes differed in only one parameter. Therefore, the effect of an individual variable cannot be isolated by comparing the experimental results of any two tubes. While this variability may introduce additional uncertainties in the quantitative analyses, it does not compromise the validity of the qualitative insights derived from the study.

Fig. 4 presents a schematic diagram of the wave tank tests for the Anaconda model. The model is positioned at the centre of the tank, with its stern secured to a carriage spanning the width of the towing tank via a wooden bracket and its bow connected to a fixed platform through a mooring line. Thus, while the bow of the Anaconda WEC exhibits six-degrees-of-freedom (6DoF), the stern remains fixed. Moreover, the top surface of the tube is located 5 cm below the free surface. An experimental snapshot is provided in Fig. 5.

It is important to highlight that although the same type of rope is used as the mooring line in all tests to restrain the motion of the tube's bow, the mooring line length and pre-tension vary, as listed in Table 3. Unfortunately, the exact pre-tension values were not directly measured during the experiments. However, based on the known pre-stretch lengths applied in each case, the relative levels of mooring pre-tension were qualitatively estimated and categorized as small, medium, and large. This enabled us to examine the influence of different pre-tension levels on the system's dynamic response. Notably, Tube 5 was tested with two different mooring lines and varying pre-tension levels. This adjustment was necessary because, when Tube 5 was subjected to an excess pressure of 6854 Pa with a shorter mooring line and higher pre-tension, the mooring line failed. To prevent mooring line failure in subsequent tests, a longer mooring line with reduced pre-tension was used.

2.3. Data acquisition and analysis

2.3.1. Measurement sensors

A series of sensors were installed on the WEC system to acquire the interested physical quantities. As indicated in Fig. 4(a), a resistance type wave probe (WP1) was positioned near the mooring point to measure the incident wave height and period. In addition, an Ultrasonic wave probe (WP2) and a differential pressure transducer (PG1) were installed on the orifice plate (see Fig. 6(a)) to measure the OWC elevation within the vertical tube and the pressure fluctuation in the air chamber, respectively.

To investigate the material behaviour, custom-made strain gauges were uniformly distributed along the flexible tube by monitoring its time-varying cross-sectional area. As shown in Fig. 6(b), the gauges are affixed circumferentially, perpendicular to the tube's length. As illustrated in Fig. 7(a), each strain gauge consists of a silicone deformable tube filled with liquid metal. The gauge is later connected to a bridge amplifier, variation in the gauge resistance can thus be determined by measuring the voltage across the gauge. As the silicone tube is elongated with the expansion of the Anaconda tube, the effective length and diameter of the liquid metal varies accordingly, leading to a linear change in electrical resistance and, consequently, a change in the voltage measured across the gauge. By measuring this voltage and using a calibrated voltage-length relationship, the extension of the strain gauge can be determined. The custom-made strain gauges, as shown in Fig. 7(b), each has a length of 265 mm. Moreover, as depicted in Fig. 3, seven strain gauges (SG1∼SG7) are distributed along the tube, with their specific positions provided in Table 4.

Due to variations in the mass of liquid metal among different strain

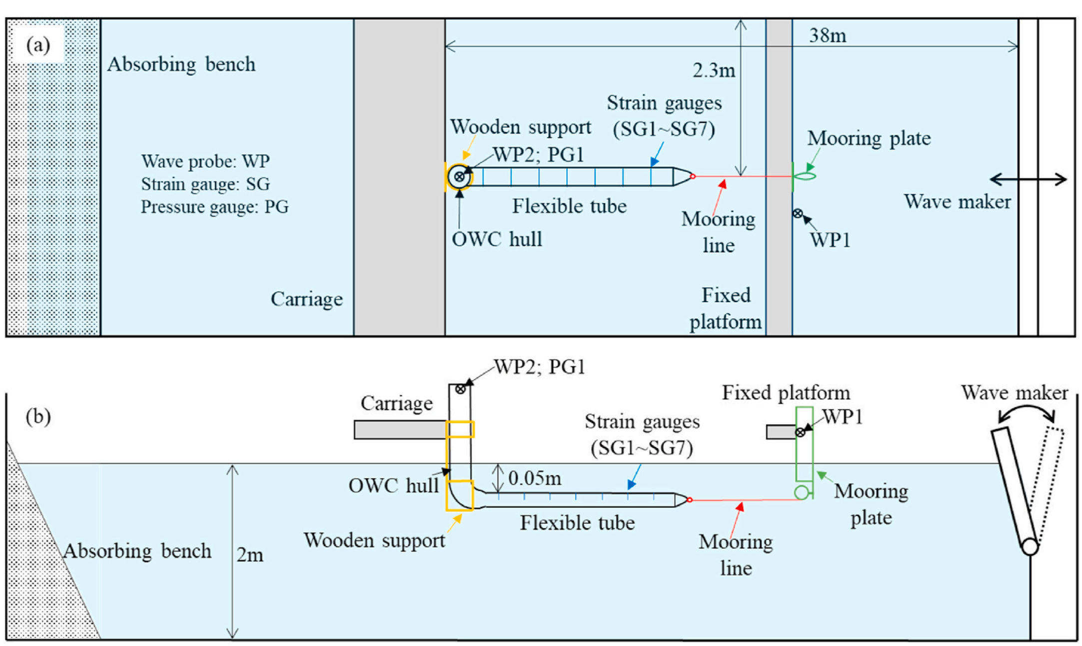

Fig. 4. Schematic of the experimental setup on a flexible tube WEC device: (a) plane view; (b) side view.

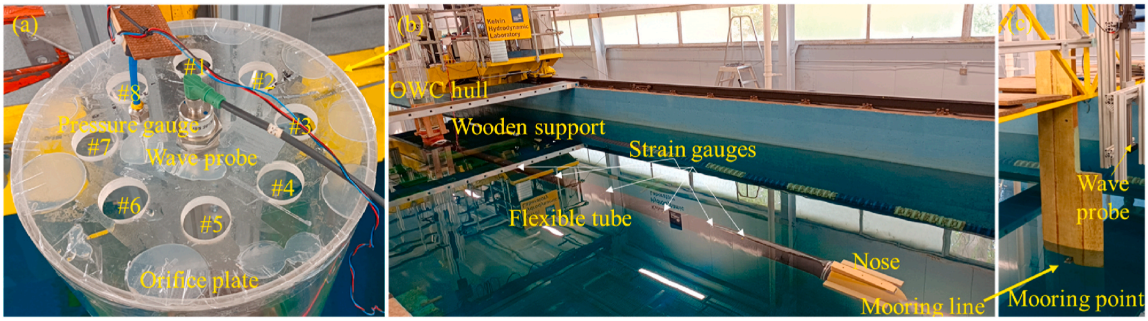

Fig. 5. Photos of (a) orifical plate on OWC hull; (b) Anaconda WEC model; (c) mooring structure.

Table 3
Configuration of mooring lines for different Anaconda models.

No.	Excess pressure (Pa)	Length (m)	Pre-tension
Tube 1	4896	1.5	Medium (0.15 m)
Tube 2	4896	2.0	Medium (0.15 m)
Tube 3	4896	3.0	Medium (0.15 m)
Tube 4	4896	2.0	Large (0.20 m)
Tube 5	4896	2.0	Large (0.20 m)
Tube 5	6854	3.5	Small (0.10 m)

gauges, calibration tests were conducted prior to their application to determine the linear relationship between voltage change and gauge extension. Specifically, each strain gauge was sequentially stretched to predetermined lengths, and the corresponding voltage was measured. The data were then fitted to the linear equation:

$$\Delta y = kV + b \tag{1}$$

where k is the slope, b is the intercept, Δy is the extension, and V is the measured voltage.

For instance, Fig. 8(a) depicts the relationship between the extension (x) and voltage (V) for Strain Gauge 1 (SG1) along with its linear fitting coefficients. Furthermore, Fig. 8(b) presents the uncertainty analysis for SG1, demonstrating that the measurement errors lie within the 95 %

Table 4
Positions of strain gauges on flexible tubes.

Position	Tube 1	Tube 2	Tube 3	Tube 4	Tube 5
Δx_b	0.57 m	0.7 m	0.6 m	0.4 m	0.4 m
Δx	0.3 m	0.9 m	0.9 m	0.7 m	0.7 m
Δx_s	0.43 m	0.6 m	0.8 m	0.4 m	0.4 m

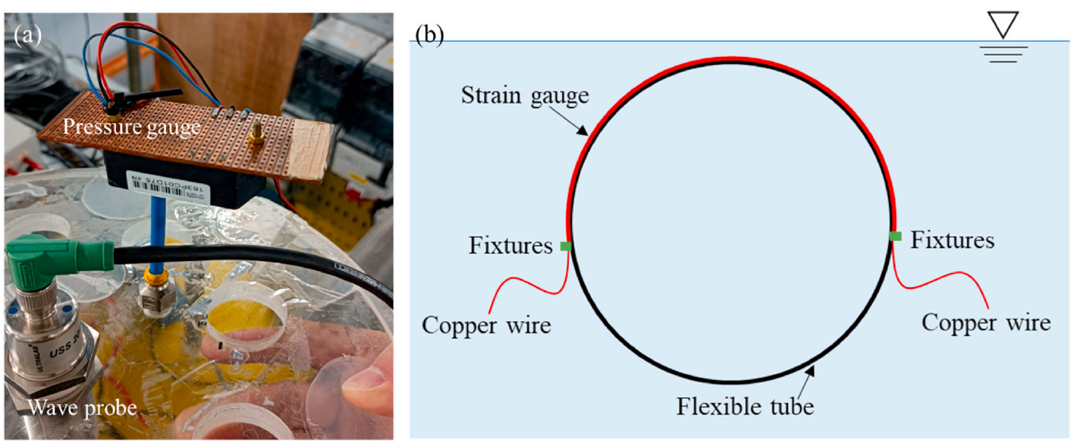

Fig. 6. (a) Photos of the pressure gauge and wave probe mounted on the orifice plate; (b) schematic diagram of strain gauge on the flexible tube.

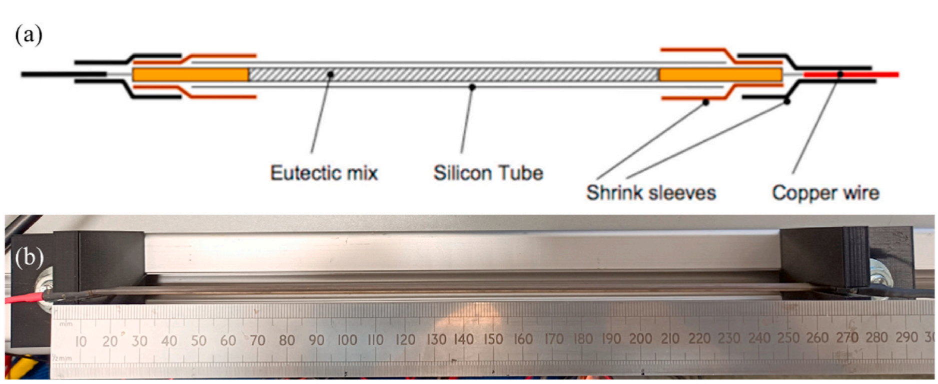

Fig. 7. (a) Schematic diagram of a strain gauge; (b) Photograph of a strain gauge.

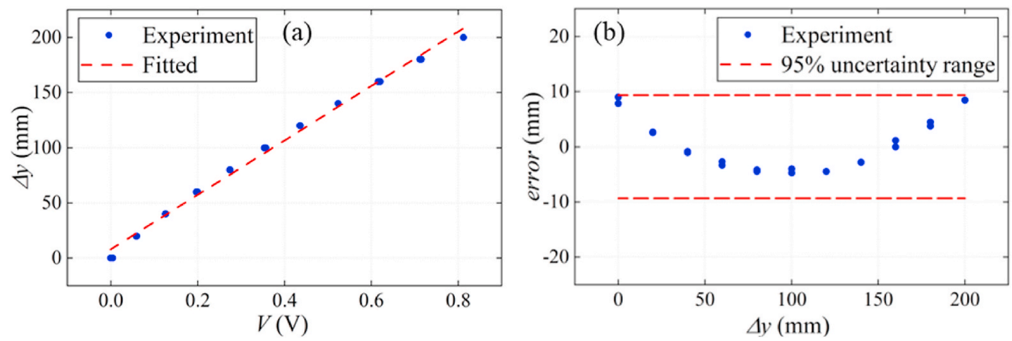

Fig. 8. Calibration results of the strain gauges: (a) voltage-displacement curve; (b) uncertainty analysis.

confidence interval. The linear fitting parameters, including the coefficient of determination (R^2), for all strain gauges are summarized in Table 5, confirming that all gauges exhibit a linear relationship between output voltage and applied extension.

2.3.2. Data analysis

To better characterize the deformation of the flexible tube's cross-section and the power output of the Anaconda WEC, the experimental data were processed as follows. As indicated by Fig. 6(b), the length of the strain gauge, l_s, is less than the circumference of the flexible tube's cross-section (with diameter D_0). The measured strain gauge length exhibits periodic variations with an amplitude Δl_s. Thus, the amplitude of the diameter variation, ΔD_0, is given by:

$$\Delta D_0 = (D_0 \cdot \Delta l_s) / l_s \tag{2}$$

In addition, a wave probe located on the orifice plate measured the time-varying OWC elevation, $\eta_o(t)$, while a pressure gauge at the same location recorded the time-varying air pressure in the chamber, $p_a(t)$. Based on these measurements, the instantaneous power output of the Anaconda WEC, $P(t)$, can be estimated as (Ning et al., 2019; Orphin et al., 2022):

$$P(t) = p_a(t) \cdot A_1 \cdot \dot{\eta}_o(t) \tag{3}$$

where $p_a(t) \cdot A_1$ is the force applied at the orifice plate, $A_1 = 0.25\,\pi D_1{}^2$ is the area of the orifice plate, $\dot{\eta}_o$ is the velocity of the OWC. Furthermore, the average power output ($\overline{P}$) of the Anaconda WEC over one wave period is given by:

$$\overline{P} = \frac{W_e}{T_w} = \frac{1}{T_w}\int_{t=0}^{t=T_w} P(t)dt \tag{4}$$

where W_e is the total energy absorbed by the Anaconda WEC during one wave period, and T_w denotes the wave period.

To evaluate the efficiency of WEC system in utilizing wave energy, the capture width (CB) is calculated as follows:

$$CB = \frac{\overline{P}}{P_w} = \frac{8\pi f_w \overline{P}}{\rho g^2 H_w{}^2} \tag{5}$$

where P_w represents the incident wave power, g is the gravitational acceleration, ρ denotes the water density, H_w is the wave height, and f_w represents the wave frequency.

2.4. Test conditions

In the present experiments, regular waves with varying parameters were investigated, with wave periods ranging from 1.11s to 6.67 s and wave amplitudes from 0.01m to 0.06 m. Detailed wave parameters are summarized in Table 6.

The experimental setup followed Froude similarity, which is widely accepted for problems involving wave-structure interaction (Bispo et al., 2022; Amouzadrad et al., 2024; Mohapatra and Soares, 2024; Mohapatra et al., 2025). This approach ensures that the dominant inertial and gravitational forces governing the hydroelastic response are properly scaled. The selected wavelengths and tube dimensions yield non-dimensional wave parameters and slenderness ratios that are consistent with those of typical full-scale Anaconda WEC systems. Therefore, the trends observed in hydroelastic behaviour and resonance characteristics are expected to be qualitatively applicable to full-scale implementations.

Assuming a geometric scale of 1:30, the corresponding prototype wave periods range from 6.08 s to 36.5 s, which encompasses most realistic ocean wave conditions. The full-scale wave amplitudes range from 0.3 m to 1.8 m, corresponding to small wave steepness values commonly encountered in operational sea states.

The PTO system is simplified to an orifice plate. By varying the number of open holes, specifically using configurations with 1, 2, 3, and 6 open holes, different levels of PTO damping were simulated. As the number of open holes increases, the PTO damping gradually decreases.

In the actual Anaconda WEC, the flexible tube is filled with

Table 6
Detailed parameters of the Anaconda models in the experimental tests.

No.	Wave period T_w (s)	Wave amplitude A_w (m)	Open holes number (PTO damping)	Excess pressure p_e (Pa)
Tube 1	1.57–5.97	0.04	1; 2; 3; 6	4896
Tube 2	1.05–6.67	0.01–0.06	1; 2; 3	4896
Tube 3	1.11–6.67	0.04	1; 2; 3	4896
Tube 4	1.11–4.00	0.04	1; 2; 3	4896
Tube 5	1.25–5.00	0.01–0.06	1; 2; 3	4896; 6854

Table 5
Summary of calibration results for the strain gauges.

	SG1	SG2	SG3	SG4	SG5	SG6	SG7
k	248.86	24.679	391.98	237.89	185.46	167.91	465.97
b	7.9821	10.495	8.9073	7.8635	7.8535	9.2147	8.8300
R^2	0.9946	0.9915	0.9949	0.9939	0.9950	0.9945	0.9900

pressurized water to enhance its deformation potential. To simplify the experimental setup, we adopted the approach used in previous studies (Chaplin et al., 2012; Mendes et al., 2014, 2017) by injecting water into the vertical tube at the stern. This procedure elevates the free surface of the vertical tube above the external free surface, thereby generating excess pressure within the horizontally oriented flexible tube in the form of hydrostatic head. According to Chaplin et al. (2012), this excess pressure significantly influences the propagation velocity of bulge waves within the flexible tube, which in turn affects the hydroelastic response of the Anaconda WEC. Thus, two levels of excess pressure were considered in this study: 4896 Pa and 6854 Pa, corresponding to hydrostatic heads in the vertical PTO tube that are 50 mm and 70 mm above the external free surface, respectively.

The selection of key design and operating parameters, including tube geometry, material properties, excess pressure, PTO damping, and wave amplitude, is guided by their expected influence on the hydroelastic response of the Anaconda WEC. Among these, bulge-wave-induced resonance is a unique dynamic feature of the Anaconda system and is primarily governed by the distensibility of the flexible tube (Chaplin et al., 2012). Variations in material properties, tube diameter, wall thickness, and internal excess pressure directly affect the tube's distensibility, thereby altering the bulge wave propagation speed and shifting the associated resonant frequency.

In contrast, parameters such as tube length are more closely related to the overall mass and inertia of the system, and thus primarily influence the natural frequencies of surge and heave motions, as well as the internal oscillation of the OWC. It should be noted, however, that several parameters affecting bulge-wave behaviour, such as tube diameter, wall thickness, material properties, and excess pressure, also contribute to the system's total mass and stiffness. As a result, these parameters may indirectly influence the resonance characteristics associated with heave, surge, and OWC modes, although their dominant effects pertain to bulge-wave resonance.

Furthermore, PTO damping and wave amplitude are included to examine their influence on the amplitude and energy capture capacity of the resonant responses. PTO damping governs the rate of energy extraction and the magnitude of internal pressure oscillations, while wave amplitude determines the strength of external excitation.

These parameters were prioritised due to their direct relevance to system dynamics and energy conversion performance. Other secondary factors, such as wave directionality and mooring system configuration, were excluded from the current test matrix in order to isolate the fundamental fluid-structure interaction mechanisms. This parameter selection framework underpins the experimental design and provides a necessary basis for interpreting the observed resonance phenomena in the subsequent analysis.

3. Material characterization

3.1. Uniaxial tensile test

Two rubber materials, NR45 and NR70, were used to fabricate the flexible tubes for the experiments. To characterize their material properties, uniaxial tensile tests were performed for both materials. Test specimens were extracted from spare material at one end of the flexible tubes, with dimensions of 25 mm in width, 200 mm in length, and 1.5 mm in thickness. Each specimen was marked with two reference lines spaced 100 mm apart. Representative specimens are shown in Fig. 9(a). Subsequently, the specimens were mounted in a tensometer (Fig. 9(b)) and gripped at the 100 mm marks.

The tensometer was programmed to perform three cycles of extension and relaxation. The tests commenced at a 50 % strain, followed by an additional 100 % extension, resulting in an overall strain range from 50 % to 150 %, which is considered a practical working range for natural rubber compounds. The grip separation rate was maintained at 100 mm/min.

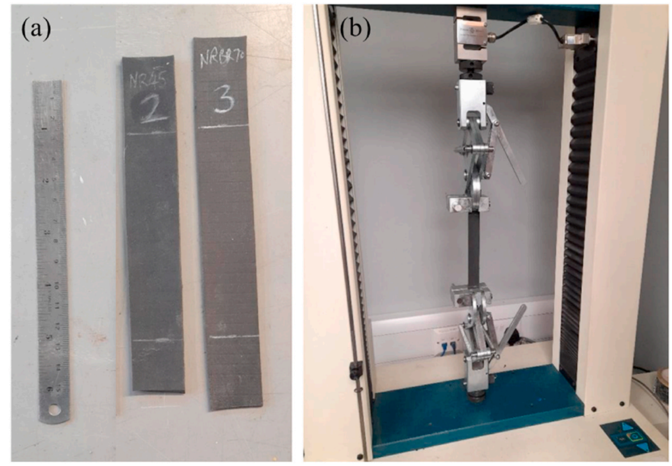

Fig. 9. (a) Specimens cut from flexible tubes; (b) Specimen mounted in the tensometer (Checkmate Flexible Engineering Ltd, 2025).

3.2. Load-extension behaviour

Fig. 10 presents the tensile test results for samples extracted from Tube 4 (NR70) and Tube 5 (NR45). The load-extension curves for the NR45 specimens nearly overlap during both loading and unloading, exhibiting an almost linear response with little hysteresis. In contrast, the NR70 specimens follow a distinct curve, showing a lower force during unloading and indicating a higher degree of hysteresis. Moreover, the NR70 specimens demonstrate increased stiffness at lower strains compared to the NR45 specimens, a difference attributable to the additives in the compound. Based on these data, the Young's modulus of the NR45 and NR70 materials are calculated. The Young's modules for the various tubes are summarized in Table 7, where the values for Tubes 1–3 were obtained previously by Checkmate Flexible Engineering Ltd. (Checkmate Flexible Engineering Ltd, 2025) via uniaxial tensile testing, and those for Tubes 4–5 were determined in the present study.

4. Results

In this section, we analyse and discuss the experimental results obtained from wave tank tests of the Anaconda model under regular wave conditions, with a particular focus on the device's resonant responses. First, the fluid-structure interaction behaviour under a representative wave condition is presented to provide a general understanding of the system's hydroelastic characteristics. Subsequently, we examine how various structural and hydrodynamic parameters influence the resonant frequencies and response amplitudes associated with different

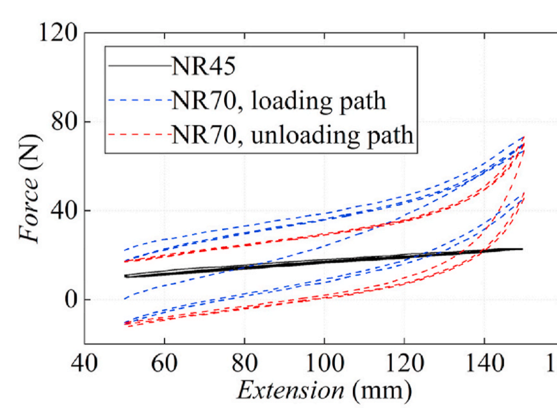

Fig. 10. Load-extension curves of flexible material samples obtained from tensile test: (a) NR45; (b) NR70.

Table 7
Detailed parameters of the Anaconda models in the experimental tests.

No.	Tube 1	Tube 2	Tube 3	Tube 4	Tube 5
Young's modulus E (MPa)	0.65	0.65	0.65	1.50	0.80

resonance modes of the device.

The system structural parameters, such as tube diameter, wall thickness, Young's modulus of the tube material, and internal excess pressure, directly affect the tube's stiffness, mass, and distensibility, and are primarily responsible for tuning the bulge-wave-induced resonance. These parameters modify the bulge wave speed, which governs the coupling between internal and external wave motions. On the other hand, tube length is more closely associated with the mass distribution and plays a significant role in determining the natural frequencies of surge and heave modes.

Additionally, the effects of PTO damping and wave amplitude are analysed. Although these parameters do not alter the resonance frequencies, they have a significant impact on the magnitude of the hydroelastic responses. PTO damping affects energy extraction efficiency and internal pressure dynamics, while wave amplitude controls the excitation input from the wave field. Together, these analyses provide insight into the dynamic response characteristics and energy capture performance of the Anaconda WEC under varying operating conditions.

4.1. FSI responses

To gain an intuitive understanding of the Anaconda WEC's operating mechanism, we selected a wave condition in which the interaction between the tube and the incident wave was pronounced (wave height A_w = 40 mm, wave frequency f_w = 0.8 Hz). In this experiment, model Tube 5 was employed under an excess pressure of 4896 Pa, and PTO damping was provided by an orifice plate with three open holes.

As illustrated in Fig. 11, where a transient experimental snapshot of the Anaconda model under regular waves is presented. Fig. 11(a) shows the oscillating water column (OWC) within the vertical tube at the device's stern, Fig. 11(b) provides an above-water view depicting the interaction between the tube and the incident wave, and Fig. 11(c) offers an underwater perspective of the tube's deformation.

When the wave passes over the tube, a pressure differential develops between its interior and exterior, inducing localized deformation and the formation of bulge waves. Notably, Fig. 11(b) reveals that the tube emerges above the water surface, a phenomenon not captured in reduced-order models (Farley et al., 2012; Chaplin et al., 2012; Babarit et al., 2017), while has been observed in our recent high-fidelity numerical studies (Huang et al., 2023, 2025). Moreover, the interaction between the tube and the incident wave generates distinct diffraction and radiation waves, and reflections from the sidewalls introduce additional nonlinear deformations of the wave surface. These complexities in the flow field around the Anaconda WEC warrant deeper investigation in numerical models.

As indicated in Fig. 11(c), the underwater view shows expansion and contraction of the tube's cross-sectional area. This structural deformation drives internal fluid motion, leading to oscillations in the OWC within the vertical tube at the stern (as seen in Fig. 11(a)), which in turn actuates the PTO (represented by the orifice plate) to produce power output.

Additionally, Fig. 12 presents the time histories of measured variables, including the incident wave elevation (η_w), the variation in tube diameter (ΔD_0) obtained from SG2, the OWC elevation (η_o), and the air chamber pressure (p_a). Under regular wave conditions, the tube's cross-sectional radius, the OWC height, and the air chamber pressure exhibit distinct periodic variations that align with the wave period.

4.2. Resonant responses

For the WEC system, the resonance response represents the condition under which power generation is maximized and the hydroelastic response is most pronounced. According to the studies by Farley et al. (2012) and Chaplin et al. (2012), the typical resonance response of the Anaconda WEC occurs when the external water wave phase speed (c_w) matches the free bulge wave speed (c_b) within the tube.

It is noted that the free bulge wave is a special case of bulge waves, referring to those that propagate naturally within the tube without external forcing, such as incident water waves or external excitations. Its

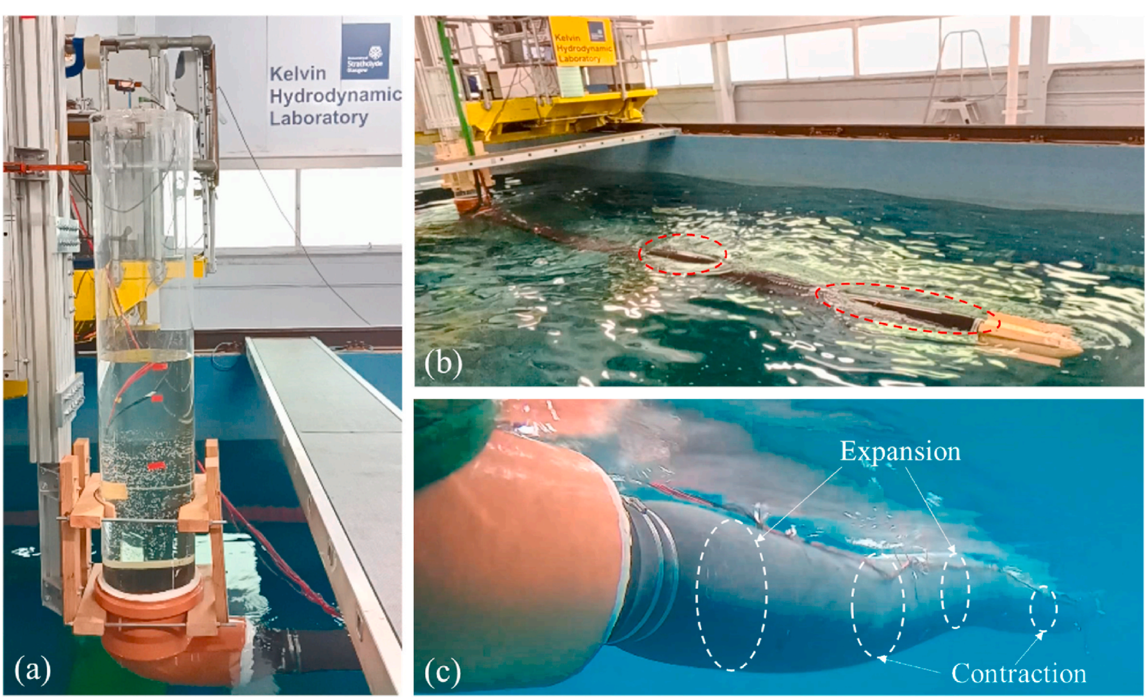

Fig. 11. Responses of the Anaconda WEC model under regular wave conditions: (a) OWC; (b) above water view; (c) underwater view.

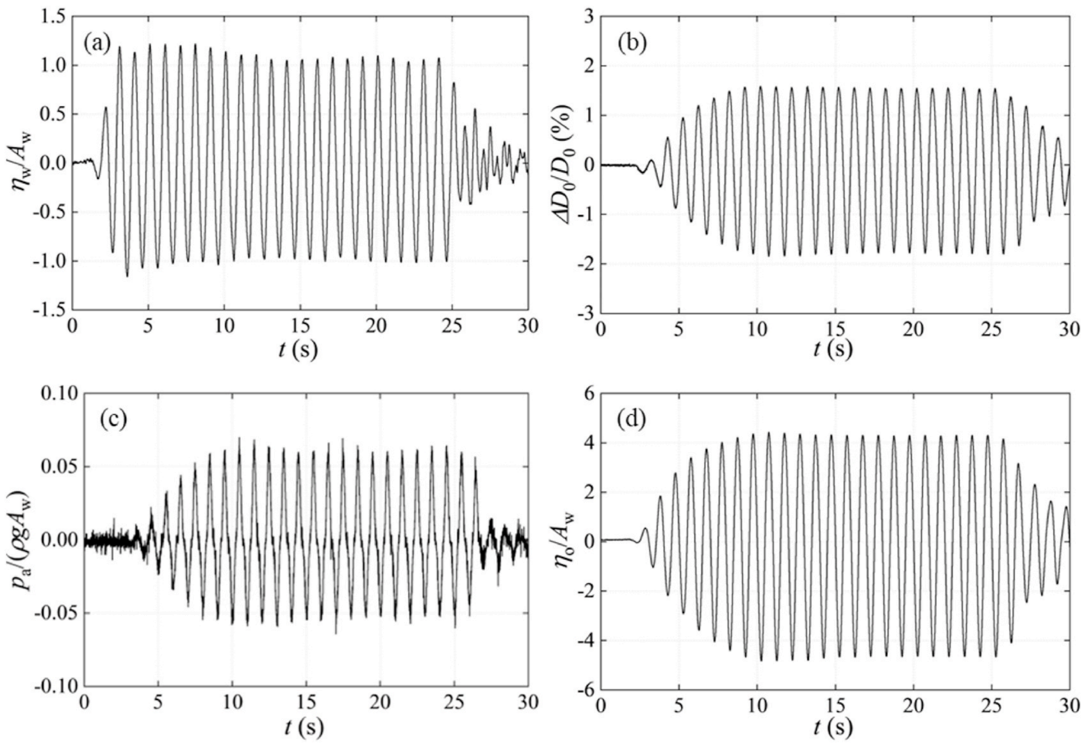

Fig. 12. Time history of different variables: (a) incident wave; (b) deformation of tube's diameter (SG 2); (c) water elevation in OWC hull; (d) air-chamber pressure.

speed is determined solely by the intrinsic properties of the flexible tube and the internal fluid, including its material, diameter, wall thickness, excess pressure, and fluid density.

According to LLW theory (Lighthill, 1978) and under the assumption that the bulge wave is non-dispersive and undamped, c_b is given by:

$$c_b = 1 \Big/ \sqrt{\rho D_t} \tag{6}$$

where ρ is the fluid density, D_t is the tube's distensibility. Assuming that the tube is incompressible with a Poisson's ratio of 0.5, D_t can be estimated by (Chaplin et al., 2012):

$$D_t = \frac{3D_0}{4Et_0} \frac{\beta(\beta - 1 + \alpha)}{\alpha - (\beta - 1)^2} \tag{7}$$

where α denotes the proportion of the tube's circumference that undergoes deformation, $\beta = D/D_0$ (with D denoting the expanded diameter under excess pressure), E is the Young's modulus of the tube.

Furthermore, based on Linear Long Wavelength (LLW) theory (Lighthill, 1978), the phase speed of gravity-driven waves on a fluid layer is given by:

$$c_w = \sqrt{\frac{g\lambda}{2\pi} \tanh\left(\frac{2\pi h}{\lambda}\right)} \tag{8}$$

where h is water depth, and λ is the wavelength.

Using above formulas, we estimated the free bulge wave speeds for five models and compared them with experimental measurements, as summarized in Table 8. In most cases, the theoretical predictions deviate from the experimental data by less than 10 %, an accuracy consistent with previous research (Heller et al., 2010; Pedley, 1980). Given the uncertainties in the uniformity of the tube material which significantly influences D_t and consequently c_b, the discrepancy is considered acceptably small. This good agreement between theory and experiment also serves as a validation of the accuracy and consistency of the experimental results. It is worth noting that for Tube 5 under an internal excess pressure of 6854 Pa, the theoretical prediction indicates the free bulge wave speed is lower than the minimum wave phase speed generated during testing where wave frequencies ranged from 0.15 Hz to 0.70 Hz. As a result, no bulge wave resonance response was observed for this configuration.

Table 8
Comparison of theoretical predictions and experimental measurements of free bulge wave speeds.

No.	Excess pressure (Pa)	Theory value (m/s)	Experimental data (m/s)	Discrepancy (%)
Tube 1	4896	2.361	2.229	−5.59
Tube 2	4896	2.096	2.311	10.24
Tube 3	4896	2.801	2.803	0.07
Tube 4	4896	2.653	2.589	−2.31
Tube 5	4896	2.846	3.034	6.60
Tube 5	6854	2.045	–	–

Besides the resonance induced by the bulge wave, our experiments also revealed additional resonant frequencies for the Anaconda WEC. Fig. 13 illustrates the Response Amplitude Operator (RAO) of the OWC in the vertical tube at the device's stern, where RAO is defined as A_o/A_w (with A_o representing the amplitude of the OWC). The RAO is plotted over a range of wave frequencies for various tested models. In these tests, the wave height was maintained at 40 mm, and PTO damping was provided by an orifice plate with one open hole (strong damping). The observed RAO peaks correspond to the resonant frequencies of the Anaconda WEC system.

The resonant frequencies, induced by the bulge wave (f_{Rb}), the surge (f_{Rs}) and heave (f_{Rh}) motions of the tube, and the OWC (f_{Ro}), are summarized in Table 9. It is clear that when the incident wave frequency approaches the natural frequency of the tube's heave motion, surge motion, or the OWC, the Anaconda WEC resonates, resulting in peak

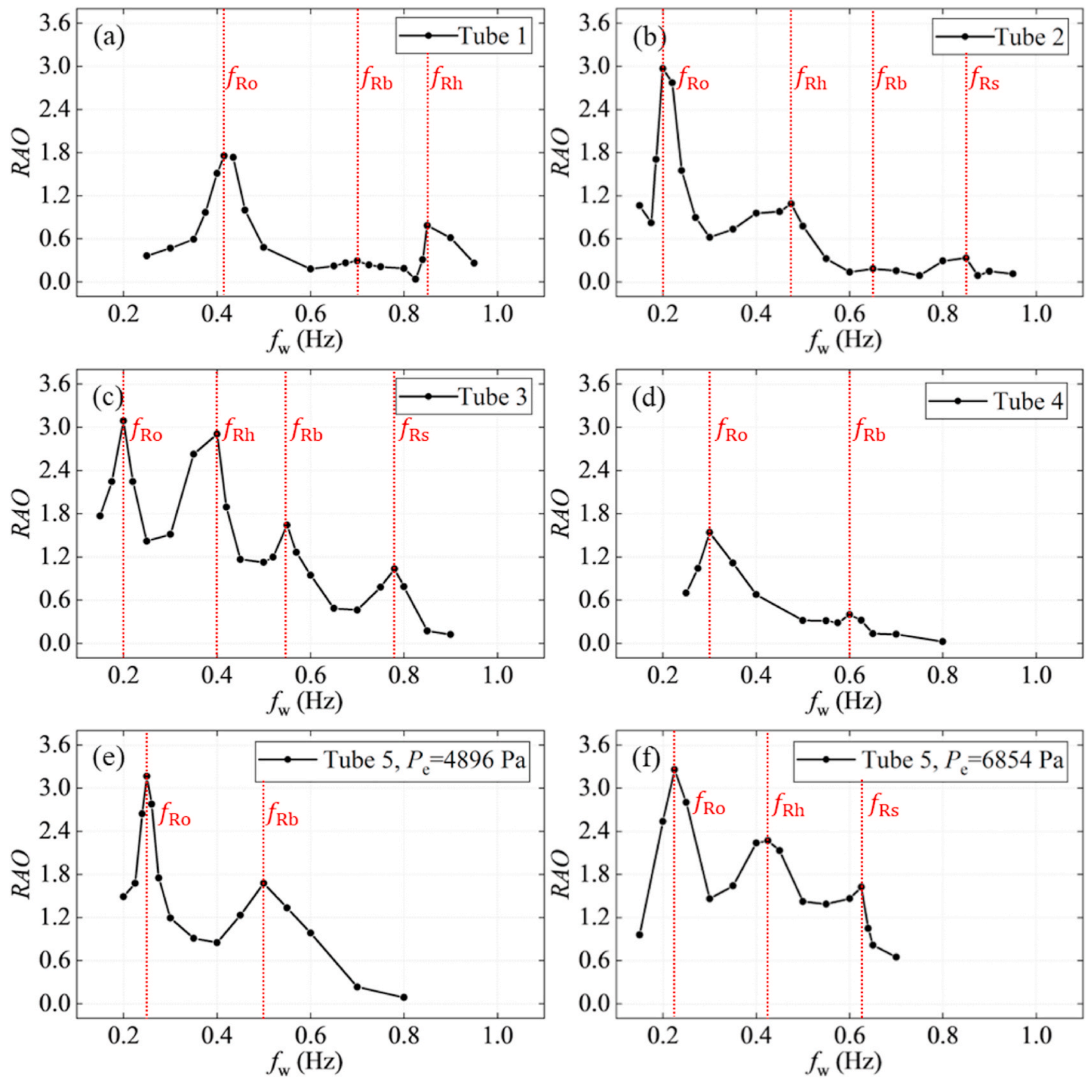

Fig. 13. RAO of OWC for various Anaconda WEC models under different wave frequencies (A_w = 40 mm, PTO damping: one hole).

Table 9
Summary of resonant frequencies in the Anaconda WEC System.

No.	Excess pressure p_t (Pa)	OWC f_{Ro} (Hz)	Bulge wave f_{Rb} (Hz)	Heave motion f_{Rh} (Hz)	Surge motion f_{Rs} (Hz)
Tube 1	4896	0.415	0.700	0.900	–
Tube 2	4896	0.200	0.675	0.475	0.850
Tube 3	4896	0.200	0.550	0.400	0.780
Tube 4	4896	0.300	0.600	–	–
Tube 5	4896	0.250	0.500	–	–
Tube 5	6854	0.225	–	0.425	0.625

energy output. Notably, these resonance phenomena have not been reported in previous studies but were clearly observed in our experiments. Moreover, the RAO peaks due to the tube's heave and surge motions were greater than those induced by the bulge wave, with the maximum RAO observed at the OWC's natural frequency.

Furthermore, Fig. 14 presents the deformation profiles along the tube length for various Anaconda models at different resonant frequencies. The variation in tube diameter ($\Delta D_0/D_0$) quantifies the bulge wave amplitude induced by both internal and external fluid loading. At frequency f_{Ro}, the amplitude is highest in the bow region and gradually decreases along the tube length towards the stern. In contrast, at frequency f_{Rb} the amplitude increases linearly along the tube, reaching its maximum in the stern region, in agreement with the observations by Farley et al. (2012) and Chaplin et al. (2012). Similarly, at frequency f_{Rh} the amplitude increases along the tube, attaining its maximum in the stern region. However, at frequency f_{Rs}, the deformation behaviour deviates from this trend. Along the tube length towards the stern,the amplitude variation is nonmonotonic and exhibits multiple peaks.

4.2.1. *Impact of geometric dimensions*

The geometric dimensions of the flexible tube, including its length, diameter, and wall thickness, are critical in determining the hydroelastic response and power output of the Anaconda WEC. To investigate these effects, we compared experimental data from various tested models. Although experimental constraints prevented the fabrication of identical tubes with only a single varying parameter, this does not preclude a meaningful qualitative analysis.

Tubes 1, 2, and 3 share the same material, diameter, PTO damping, and wave conditions, differing only in tube length and wall thickness. As tube length increases, the mass of water contained within the tube rises

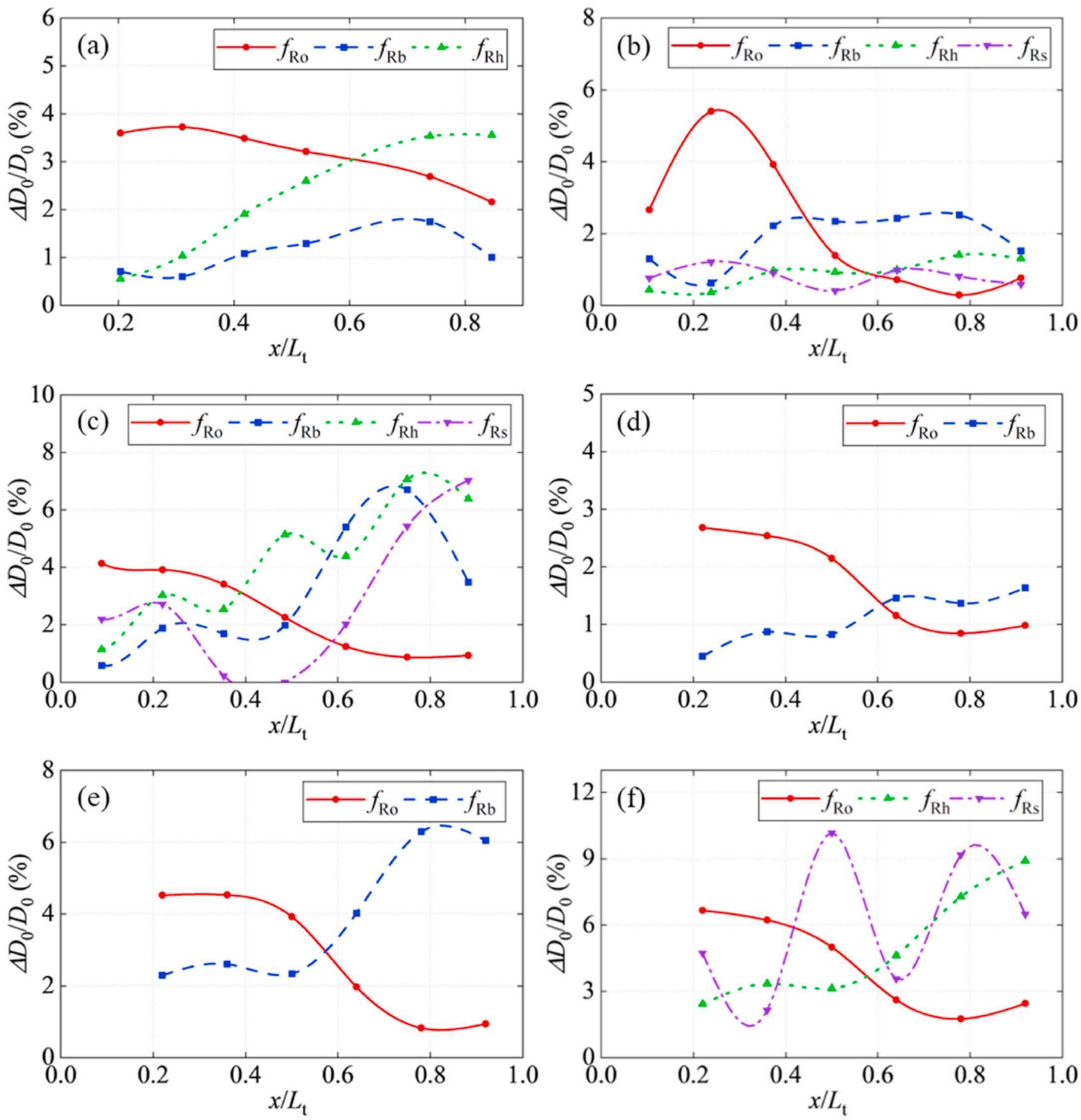

Fig. 14. Variation amplitude of tube diameter for various Anaconda WEC models under different resonant frequencies (A_w = 40 mm, PTO damping: one hole): (a) Tube 1; (b) Tube 2; (c) Tube 3; (d) Tube 4; (e) Tube 5, p_e = 4896 Pa; (f) Tube 5, p_e = 6854 Pa.

significantly, leading to a marked reduction in f_{Ro} from 0.415 Hz in Tube 1 to 0.2 Hz in Tube 2. Similarly, f_{Rh} decreases from 0.9 Hz in Tube 1 to 0.475 Hz in Tube 2. It is important to note that mooring line tension, which was not measured in our experiments, also affects f_{Rh} and requires further investigation in the future. According to Eqs. (6) and (7), tube length does not affect f_{Rb}. The differences in f_{Rb} between Tubes 1 and 2 are mainly attributable to the differences in wall thickness, which will be discussed subsequently. Fig. 15 shows the energy absorbed (W_e) within one wave period and the time-averaged power output ($\overline{P}$) for Tubes 1–3 across various wave frequencies. Comparison between Tubes 1 and 2

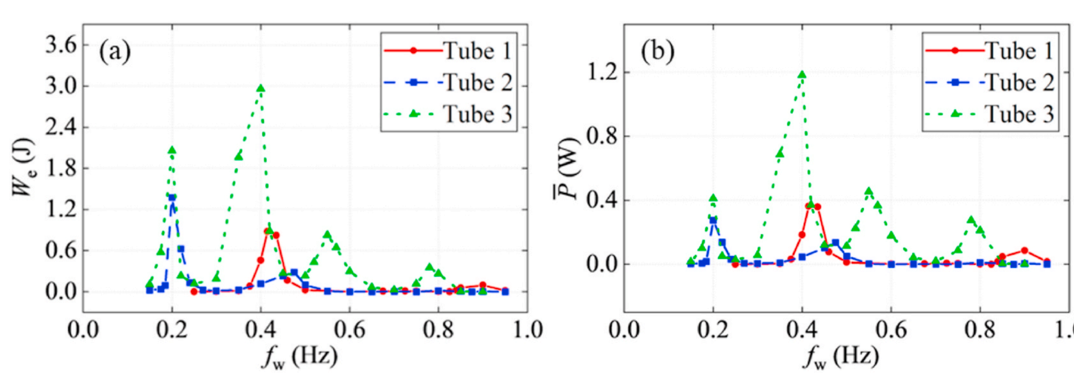

Fig. 15. Power output of Anaconda WEC models across different wave frequencies (A_w = 40 mm, PTO damping: one hole): (a) energy generated within one wave period; (b) time-averaged power output.

indicates that increasing tube length enhances W_e at f_{Ro}, although $\overline{P}$ decreases due to the longer period. Additionally, the power performance at f_{Ro} and f_{Rh} is clearly superior to that at f_{Rs} and f_{Rb}.

The influence of wall thickness is primarily observed in f_{Rb}. As indicated by Eqs. (6) and (7) and corroborated by the theoretical predictions of c_w in Table 8, an increase in wall thickness leads to a higher c_b, thereby reducing f_{Rb}. For instance, when the wall thickness increases from 2.2 mm (Tube 2) to 3.5 mm (Tube 3), f_{Rb} decreases from 0.675 Hz to 0.55 Hz. However, despite Tube 1 is thinner (2.6 mm) than Tube 2, its resonant frequency f_{Rb} (0.7 Hz) is higher. This discrepancy may be attributed to the small difference in wall thickness combined with uncertainties in experimental measurements. Under the current configuration, our general observation is that wall thickness appears to have little effect on f_{Ro}, with both Tube 2 and Tube 3 exhibiting an f_{Ro} of 0.2 Hz.

In contrast, the surge (f_{Rs}) and heave (f_{Rh}) resonant frequencies are influenced by the mooring line. The differences in f_{Rs} and f_{Rh} between Tubes 2 and 3, as listed in Table 9, are primarily due to variations in mooring line length. Although both tubes used rope moorings, tube 3 has a longer mooring line, resulting in lower stiffness in the surge and heave directions. This reduction in stiffness leads to greater motion amplitudes, which in return significantly increases the OWC's RAO for Tube 3 at f_{Rs} and f_{Rh}, as shown in Fig. 13(b)~(c), which in turn led to higher energy generation and power output at these frequencies, as presented in Fig. 15. Notably, the performance of Tube 3 indicates that the power output at f_{Rh} is significantly higher than at other resonant frequencies, underscoring the importance of accurately predicting f_{Rh} for improving numerical models of the Anaconda WEC.

Regarding the influence of tube diameter, although the diameters of Tubes 1–3 differ from those of Tubes 4–5, the accompanying differences in other parameters (e.g., Young's modulus) prevent an isolated discussion of diameter effects. However, according to Eqs. (6) and (7), an increase in tube diameter leads to a decrease in c_w and a consequent increase in f_{Rb}.

4.2.2. Impact of flexible material

The impact of flexible material properties was investigated by comparing Tube 4, constructed from NR70, and Tube 5, made from NR45. Both models operated under the same excess pressure (p_e) of 4896 Pa, with identical PTO damping (one hole) and wave conditions (A_w = 40 mm). It should be noted that the thickness of Tube 5 is twice that of Tube 4.

In the perspective of resonant frequencies, when the flexible material is changed from NR70 to NR45, both f_{Ro} and f_{Rb} decrease. This occurs because the Young's modulus of NR45 is only 53 % of that of NR70. Given the same p_e, Tube 5 deforms more, leading to an increased internal water volume and, consequently, a greater mass, which results in a lower f_{Ro}. In addition, Eqs. (6) and (7) show that an increase in Young's modulus results in a higher c_b and a decrease in f_{Rb}, which is similar to the effect of tube thickness. Although Tube 5 has twice the thickness of Tube 4, its Young's modulus is lower. Considering both factors, c_b increases, thus f_{Rb} decreases. Furthermore, Tube 5 has lower stiffness and exhibits more pronounced deformation, which leads to a higher RAO for the OWC. As a result, both the energy generated (W_e) and the time-averaged power output ($\overline{P}$) at f_{Ro} and f_{Rb} are greater for Tube 5 than for Tube 4, as indicated by Fig. 16. In addition, the shorter mooring line and higher pre-tension for Tube 4 and 5 under p_e = 4896 Pa increased the system's stiffness in both surge and heave directions, resembling conditions observed in previous experiments with the bow fixed (Farley et al., 2012; Chaplin et al., 2007a, 2007b, 2012; Heller et al., 2010). This configuration resulted in natural frequencies for surge and heave motions that exceeded the wave frequency range wave frequency range generated during the experiment. Consequently, these resonance phenomena were not captured.

4.2.3. Impact of excess pressure

To investigate the effect of excess pressure, we compared the experimental results for Tube 5 under two conditions, p_e = 4896 Pa and 6854 Pa, while keeping all other parameters, including PTO damping and wave conditions, constant.

An increase in p_e leads to larger initial tube deformation, which in turn increases the mass of the OWC. As a result, f_{Ro} decreases, as summarized in Table 9. Furthermore, the overall mass of the Anaconda model increases with higher p_e, leading to reduced natural frequencies for both surge motion (f_{Rs}) and heave motion (f_{Rh}). This phenomenon explains the occurrence of surge- and heave-induced resonances at p_e = 6854 Pa, in contrast to their absence at p_e = 4896 Pa. Another contributing factor is that at p_e = 4896 Pa, the mooring line was relatively short and under high pre-tension, resulting in its failure during testing. In contrast, the tests at p_e = 6854 Pa employed a longer mooring line with lower pre-tension to prevent such failures.

Excess pressure also significantly affects f_{Rb}. According to Chaplin et al. (2012) for a flexible tube made of homogeneous, deformable material, the relationship between internal excess pressure and tube deformation is given by:

$$p_e = \frac{2Et_0}{3}\frac{(D - D_0)}{D^2} \tag{7}$$

Combining this equation with Eqs. (6) and (7) reveals that as p_e increases, c_w decreases, thereby reducing f_{Rb}. Specifically, when p_e increases from 4896 Pa to 6854 Pa, the predicted c_b decreases from 2.846 m/s to 2.045 m/s. Since this predicted value is lower than the water wave phase speeds generated during the experiments, bulge wave-induced resonance was not observed at p_e = 6854 Pa.

Furthermore, as shown in Fig. 16, increasing p_e significantly enhances the energy generation (W_e) and time-averaged power output ($\overline{P}$) of the Anaconda WEC system at frequencies f_{Ro}, f_{Rh}, and f_{Rs}. Notably, the power output at f_{Rh} exceeds that at f_{Ro}, indicating that allowing freedom

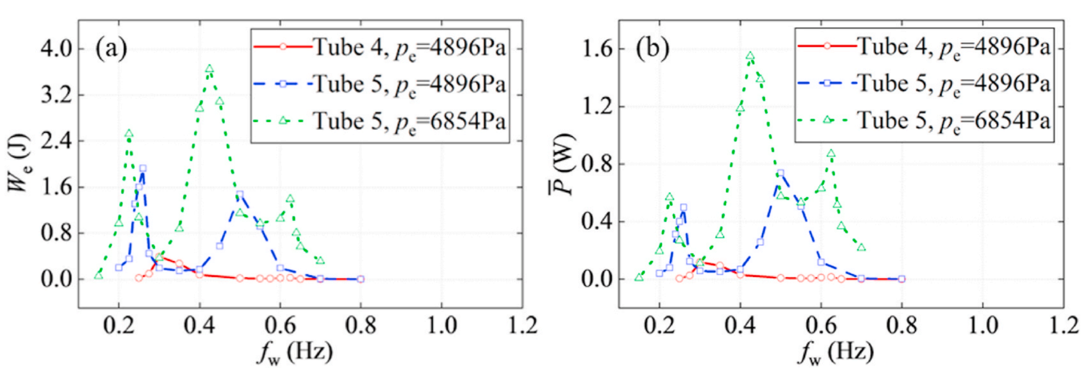

Fig. 16. Power performance of Anaconda WEC models under different wave frequencies (A_w = 40 mm, PTO damping: one hole): (a) energy generated within one wave period; (b) time-averaged power output.

in the bow motion contributes positively to power generation. This finding highlights the importance of considering motion-induced resonant responses when evaluating the performance of the Anaconda WEC system.

4.3. Influence of PTO damping

The variation in PTO damping was achieved by altering the number of open holes in the orifice plate, as seen from Fig. 5(a). Four configurations were considered: 1 hole, 2 holes, 3 holes, and 6 holes. As the number of open holes increases, the PTO damping gradually decreases. All models operated under an excess pressure of 4895 Pa and a wave height of 40 mm.

Fig. 17 compares the OWC's RAOs and the energy generated per wave period (W_e) at different frequencies for the five models with four PTO damping conditions. The results indicate that while PTO damping does not affect the resonant frequency of the Anaconda WEC, the amplitude of the RAO decreases as PTO damping increases. In addition, the energy output increases with increasing PTO damping, which suggests that the PTO damping values used in these tests are lower than the device's optimal damping. These observations were consistent across all models and were independent of variations in tube geometrical dimensions or material properties.

4.4. Influence of wave amplitude

The influence of wave amplitude on the Anaconda WEC system is also investigated. We analysed the dynamic responses for Tube 2 at the frequency f_{Ro} (0.2 Hz) and for Tube 5 at the frequency f_{Rb} (0.5 Hz) under different wave amplitudes; the detailed test conditions are summarized in Table 10.

Fig. 18 presents the deformation profiles along the tube length for various Anaconda models at different wave amplitudes. While the wave amplitude does not affect the deformation mode of the tube, the deformation magnitude gradually increases as the wave amplitude increases.

Additionally, as wave amplitude increases, viscous damping also increases, leading to greater energy dissipation and, consequently, a reduction in the RAO of the OWC, as illustrated in Fig. 19(a). Moreover, the amplitude of the air-chamber pressure (p_a) also increases with wave amplitude, as shown in Fig. 19(b). Notably, this increase is nonlinear. Table 11 quantifies this nonlinearity by comparing the relative increase in wave height and air-chamber pressure amplitude, demonstrating that pressure amplitude grows disproportionately faster than wave height. This implies that under the current configuration, doubling the wave height results in a more than twofold increase in air-chamber pressure amplitude.

Furthermore, both the time-averaged power output ($\overline{P}$) and the capture width (CB) of the WEC system increase with wave height, as shown in Fig. 19(c) and (d). It is important to note that the nonlinear increase in air-chamber pressure amplitude is the primary reason for the observed increase in CB with wave amplitude.

Notably, these phenomena remain consistent regardless of the selected frequency (0.2 Hz and 0.5 Hz) or the specific Anaconda model (Tube 2 and Tube 5).

5. Discussions

5.1. Mode coupling effects and nonlinear interactions

The dynamic behaviour of the Anaconda WEC involves multiple interacting response modes, including bulge waves, heave and surge motions, and oscillations of the OWC. While the present analysis primarily focuses on identifying the resonant characteristics associated with variations in system parameters, several experimental observations suggest the presence of modal coupling and potential nonlinear interactions among these modes.

For instance, the OWC RAO at the bulge wave resonant frequency is noticeably larger for Tube 3 than for Tube 2, as shown in Fig. 13(b) and (c). This enhancement is likely attributable to the stronger heave motion observed in Tube 3, which may have amplified the bulge wave resonance through dynamic coupling. Furthermore, Fig. 13(a), (b), and (e) indicate that when the bulge wave resonant frequency lies close to the natural frequency of the OWC, the RAO under bulge wave excitation tends to increase significantly. These findings suggest that cross-modal coupling between bulge wave and OWC modes may occur under frequency-aligned conditions and large response amplitudes.

Although the experiments were not specifically designed to quantify nonlinear effects, no evident bifurcations or harmonic distortions were observed in the time histories. Most test configurations demonstrated a proportional relationship between wave amplitude and system response, indicating that the WEC generally operated within a near-linear dynamic regime.

That said, even though the wave and structural conditions were carefully selected to represent full-scale sea states, real-world deployment scenarios may involve higher hydrodynamic loads, long-term material degradation, and additional environmental forces (e.g., currents, irregular waves). These could push the system further into nonlinear response regimes. Under such conditions, interactions between bulge wave dynamics and global 6DoF motions may lead to complex coupled responses that are not fully captured in the present experimental campaign.

Moreover, although no distinct lateral deformation patterns, such as snaking modes, were observed during testing, their potential presence and associated energy dissipation mechanisms may become more prominent in longer systems or under oblique wave incidence. All experiments in this study were conducted under head wave conditions, which predominantly excite axial modes. The finite length of the experimental model and the constraints imposed by the mooring system may also have suppressed higher-order lateral responses. These aspects will be further investigated in future work through targeted numerical simulations and extended experimental configurations.

5.2. Experimental uncertainties

Despite the careful design and execution of the experimental campaign, various sources of uncertainty inevitably influence the accuracy and repeatability of the measured results. Although the primary focus of this study is on the qualitative trends and comparative analysis across different model configurations, it is important to acknowledge and assess the main sources of experimental uncertainty.

One major source arises from the calibration of the strain gauges used to measure the tube's circumferential strain and, by extension, its cross-sectional deformation. Sensor drift and calibration errors may introduce deviations in the reconstructed tube geometry, especially under low strain conditions. In addition, minor inconsistencies in the material properties and fabrication quality of the elastic tube may affect its local stiffness, leading to slight variations in deformation response along the tube length.

Another source of uncertainty stems from the internal excess pressure applied within the flexible tube. During testing, minor leakage was observed in some tube models, which required periodic water refilling to maintain the desired internal pressure. While pressure levels were closely monitored, small variations may still have occurred between repeated runs, potentially affecting the bulge-wave propagation speed and the associated resonant frequency.

Variations in wave conditions also contribute to uncertainty. These include small inconsistencies in wave amplitude and phase due to wavemaker precision and the presence of wave reflections or residual disturbances in the tank. Such variability may influence the repeatability of the measured tube response and the calculated RAOs.

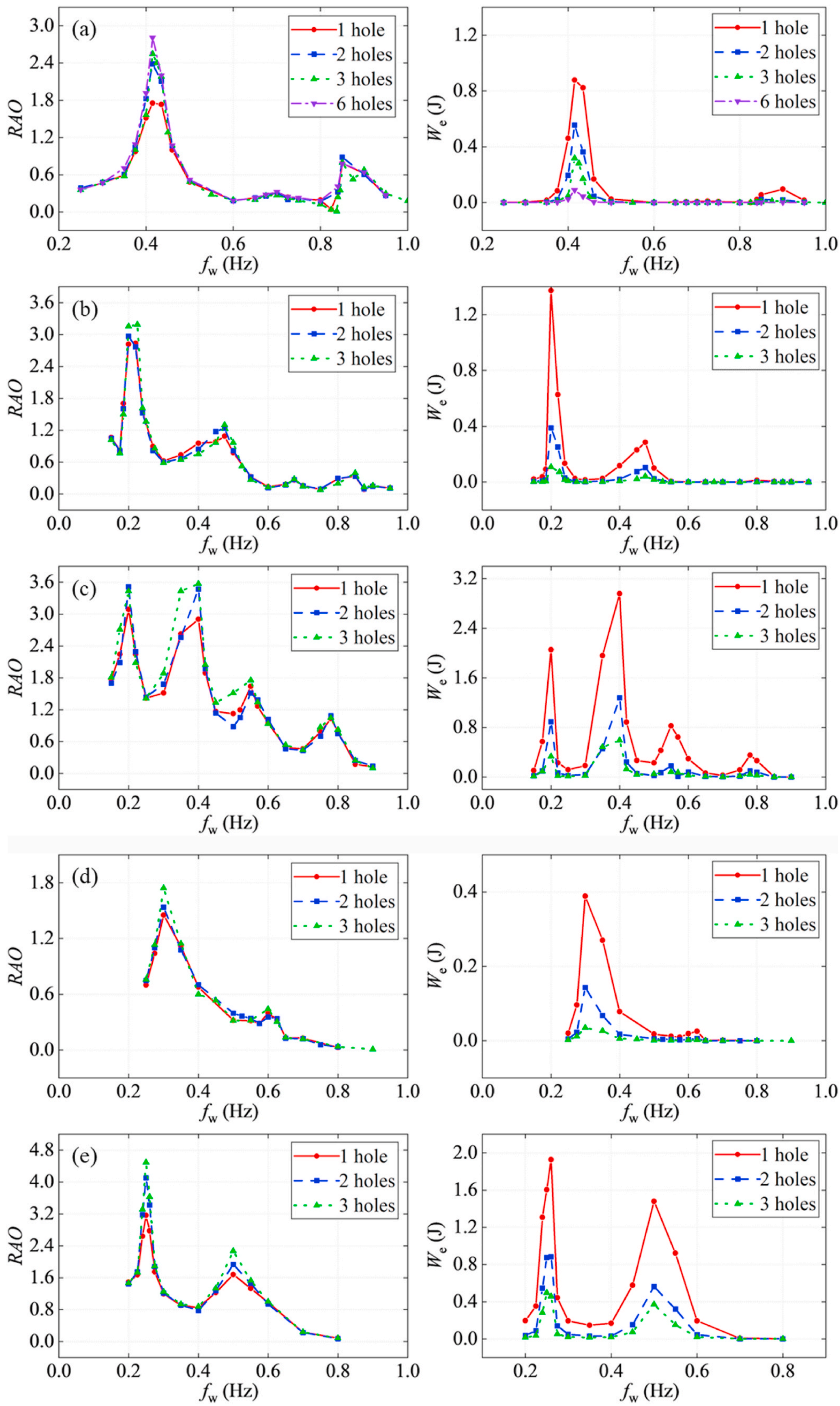

Fig. 17. OWC's RAO and energy generation of Anaconda WEC models under different wave frequencies (A_w = 40 mm, p_t = 4896 Pa): (a) Tube 1; (b) Tube 2; (c) Tube 3; (d) Tube 4; (e) Tube 5.

Table 10
Test conditions for the analysis of the impact of wave amplitudes.

No.	Wave frequency f_w (Hz)	Wave amplitude A_w (m)	Open holes number (PTO damping)	Excess pressure p_e (Pa)
Tube 2	0.20	0.01–0.06	1	4896
Tube 5	0.50	0.01–0.06	3	4896

Although a full uncertainty quantification is beyond the scope of this work, we estimate that the combined effect of these factors may introduce uncertainties of less than 10 % in the measured deformation and internal pressure data. These factors have been taken into account in the interpretation of results, particularly in the comparative analysis across different model configurations.

5.3. Experimental and analysis limitations

While the present study provides valuable insights into the hydroelastic performance of the Anaconda WEC, several limitations of the experimental setup and analysis should be acknowledged.

First, due to manufacturing constraints and the limited availability of tubes, it was not feasible to vary individual design parameters independently across different test models. As a result, the current test matrix does not follow a strict single-variable approach, limiting the ability to isolate and quantify the influence of each parameter. The analysis therefore focuses on identifying dominant response trends and qualitatively evaluating the sensitivity of the system to combined design and operational changes.

Secondly, the stiffness and pre-tension of the mooring lines were not directly measured during testing, which further limits the ability to quantify the mooring system's influence on the hydroelastic response. Although mooring effects were observed to significantly affect the system's dynamic behaviour with certain configurations, the present

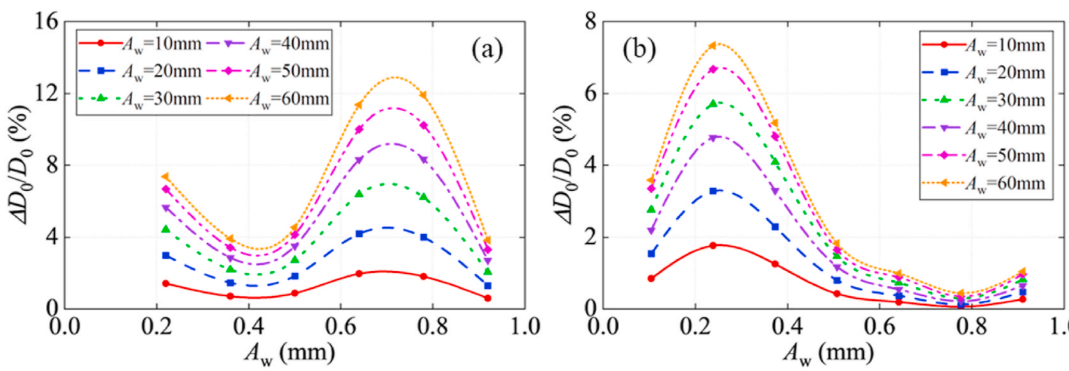

Fig. 18. Variation amplitude of tube diameter for various Anaconda WEC models under different wave amplitudes: (a) Tube 2, $f_w = 0.2$ Hz, PTO damping: one hole; (b) Tube 5, $f_w = 0.5$ Hz, PTO damping: three holes.

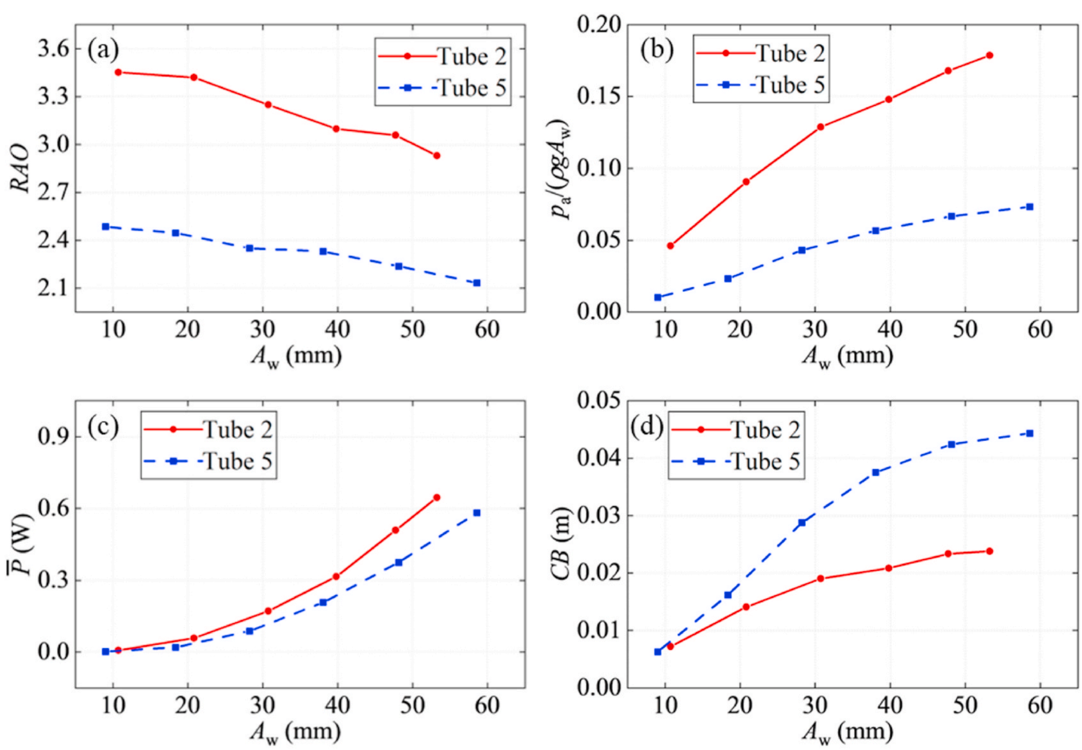

Fig. 19. Hydrodynamic responses and power generation of Anaconda WEC models under different wave amplitudes: (a) OWC's RAO; (b) energy generated per wave cycle; (c) time-averaged power output; (d) capture width.

Table 11
Variation of air-chamber pressure amplitude with amplitude.

Anaconda model	i	Wave amplitude $A_{w,i}$ (mm)	Pressure amplitude $A_{p,i}$ (Pa)	$R_w = A_{w,i}/A_{w,i-1}$	$R_p = A_{p,i}/A_{p,i-1}$	R_p/R_w
Tube 2	1	10	4.84	–	–	–
	2	20	18.48	2.00	3.82	1.91
	3	30	38.72	1.50	2.10	1.40
	4	40	57.69	1.33	1.49	1.12
	5	50	78.49	1.25	1.36	1.09
	6	60	93.17	1.20	1.19	0.99
Tube 5	1	10	0.90	–	–	–
	2	20	4.19	2.00	4.67	2.34
	3	30	11.90	1.50	2.84	1.89
	4	40	21.10	1.33	1.77	1.33
	5	50	31.39	1.25	1.49	1.19
	6	60	41.96	1.20	1.34	1.12

analysis remains qualitative in this regard.

Finally, while we acknowledge the utility of non-dimensional analysis for enhancing the generality and scalability of experimental findings, the strong coupling between geometric, material, pressure, and wave-related parameters made it difficult to construct meaningful dimensionless groups that fully capture the system's dynamics. As such, results are presented in dimensional form to preserve clarity and avoid potentially misleading interpretations. Nevertheless, we recognize the importance of developing a unified non-dimensional framework in future work. This will be pursued through the ongoing development of a high-fidelity numerical model, which will enable systematic parametric studies and the formulation of appropriate scaling relationships to support the generalized interpretation and design optimization of flexible wave energy converters such as the Anaconda WEC.

6. Conclusions

In this study, the hydroelastic responses of the Anaconda WEC system were systematically investigated through scaled model testing. A series of wave tank experiments were conducted using five scaled models, each with variations in tube geometry, material properties, excess pressure, and PTO damping. Measurements of tube deformation and PTO response were used to assess the device's hydroelastic performance. Furthermore, the FSI responses of the Anaconda WEC were examined, with a particular focus on the influence of key parameters, including tube geometry, flexible material properties, excess pressure, PTO damping, and wave amplitude, on the resonant responses of the WEC.

Our observations indicate that resonance in the Anaconda WEC system occurs not only when the external water wave phase speed matches the free bulge wave speed but also at the natural frequencies associated with the tube's heave and surge motions, as well as the OWC's natural frequency The primary factors influencing the bulge wave resonant frequency are the intrinsic properties of the flexible tube and the excess pressure. For instance, increasing the tube material stiffness or thickness, or reducing the tube diameter and excess pressure, raises the free bulge wave speed, thereby requiring a higher external wave phase speed for resonance and ultimately lowering the bulge wave-induced resonant frequency. In contrast, the mass of the Anaconda model, affected by parameters such as tube length and excess pressure, plays a critical role in determining the resonant frequencies associated with the tube's surge and heave motions, as well as the inherent resonance of the OWC; increases in these parameters result in a greater system mass and lower resonant frequencies. Moreover, the spatial deformation of the tube, characterized by the bulge wave amplitude, exhibited distinct modal patterns under different resonant conditions. At the bulge wave-induced resonant frequency and heave motion-induced resonant frequency, the amplitude increases along the tube length, whereas at the natural frequency of the OWC, it decreases, and at surge motion-induced resonant frequency, the deformation displays higher-order modal characteristics rather than a monotonic variation. Although PTO damping and wave amplitude did not alter the resonant frequencies, increasing PTO damping (within a suboptimal range) and wave amplitude amplified the resonant response, thereby enhancing the device's power output. Notably, under the current configuration, the resonant response amplitudes and power outputs at the natural frequencies of OWC, heave and surge motions exceeded those at bulge wave-induced wave frequency, underscoring the importance of accounting for motion- and OWC-induced resonances when evaluating the performance of the Anaconda WEC system numerically. Also provides a design guide on how to maximise the power capture performance of Anaconda WEC, i.e. less restriction in the bow motion leads to a wider capture bandwidth.

This study advances our understanding of the hydroelastic behaviour of the Anaconda WEC system under various configurations, which is critical for optimizing its design, particularly in terms of adjusting resonant frequencies to better accommodate the wave conditions at potential deployment sites and improve device efficiency. In particular, the investigation of resonance behaviour and hydroelastic responses is intended to serve as a reference for validating numerical models and informing the design of full-scale systems. Furthermore, the extensive experimental data provide a solid foundation for the development and calibration of future simulation tools.

However, due to practical limitations, such as the simultaneous variation of multiple parameters across different models, the current results do not support precise quantitative analysis of individual parameter effects. In addition, the influence of the mooring line on resonance behaviour is not anticipated during the initial experimental design. Future tests will include a more systematic assessment of individual parameter effects, including the contribution of the mooring system. Moreover, while this study primarily focuses on identifying qualitative trends, we acknowledge the importance of developing a unified non-dimensional framework to better characterize the coupled hydroelastic behaviour of the Anaconda WEC. This will be addressed in future work through the validation of a numerical model, enabling the construction of physically meaningful dimensionless groups to support more generalized interpretation and full-scale design optimization.

It is also important to acknowledge two inherent engineering challenges associated with the Anaconda WEC system. First, scaling up the flexible thin-tube structure while maintaining its hydroelastic performance poses significant difficulties, particularly in preserving geometric stability and dynamic similarity at larger scales. Second, optimizing the hydraulic PTO system remains a complex task, as it involves balancing efficiency, reliability, and responsiveness to unsteady internal flows within a compliant structure. These challenges warrant further investigation to ensure the practical viability of the Anaconda WEC in large-scale deployments.

CRediT authorship contribution statement

Yang Huang: Writing – review & editing, Writing – original draft, Visualization, Validation, Methodology, Investigation, Formal analysis, Data curation, Conceptualization. **Qing Xiao:** Writing – review & editing, Validation, Supervision, Resources, Project administration, Methodology, Investigation, Funding acquisition, Formal analysis, Conceptualization. **Saishuai Dai:** Writing – review & editing, Validation, Software, Investigation, Formal analysis, Data curation, Conceptualization. **Lin Cui:** Writing – review & editing, Funding acquisition. **Liu Yang:** Writing – review & editing, Funding acquisition. **Saeid Lotfian:** Writing – review & editing, Investigation, Conceptualization. **Farhad Abad:** Writing – review & editing, Conceptualization. **Guillermo Idarraga:** Writing – review & editing, Conceptualization. **Feargal Brennan:** Funding acquisition, Conceptualization.

Declaration of competing interest

The authors declare that they have no known competing financial interests or personal relationships that could have appeared to influence the work reported in this paper.

Acknowledgements

This research was supported by an Engineering and Physical Sciences Research Council (EPSRC) Grant "Bionic Adaptive Stretchable Materials for WEC (BASM-WEC)" (EP/V040553/1). The authors extend their sincere gratitude to Checkmate Flexible Engineering Ltd. for providing the experimental materials and equipment, and to Mark Prentice for his invaluable technical guidance.

References

Aderinto, T., Li, H., 2018. Ocean wave energy converters: status and challenges. Energies 11 (5), 1250.

Amouzadrad, P., Mohapatra, S.C., Soares, C.G., 2024. Review of recent developments on the hydroelastic response and gap resonance of multi-body floating structures. Ocean. Eng. 313, 119398.

Ang, T.Z., Salem, M., Kamarol, M., Das, H.S., Nazari, M.A., Prabaharan, N., 2022. A comprehensive study of renewable energy sources: classifications, challenges and suggestions. Energy Strategy Rev. 43, 100939.

Babarit, A., Singh, J., Mélis, C., Wattez, A., Jean, P., 2017. A linear numerical model for analysing the hydroelastic response of a flexible electroactive wave energy converter. J. Fluid Struct. 74, 356–384.

Bispo, I.B.S., Mohapatra, S.C., Soares, C.G., 2022. Numerical model of a WEC-Type attachment of a moored submerged horizontal set of articulated plates. Trends 335–344. Maritime Technology and Engineering.

Chaplin, J.R., Farley, F.J.M., Rainey, R.C.T., 2007a. Power conversion in the ANACONDA WEC. In: Proc 22nd Intl. Workshop on Water Waves and Floating Bodies, pp. 29–32.

Chaplin, J.R., Farley, F.J.M., Prentice, M.E., Rainey, R.C.T., Rimmer, S.J., Roach, A.T., 2007b. Development of the ANACONDA all-rubber WEC.

Chaplin, J.R., Heller, V., Farley, F.J.M., Hearn, G.E., Rainey, R.C.T., 2012. Laboratory testing the anaconda. Philos. Trans. R. Soc. A Math. Phys. Eng. Sci. 370, 403–424, 1959.

Checkmate flexible engineering ltd. https://www.strath.ac.uk/engineering/navalarchitectureoceanmarineengineering/workingwithbusinessorganisations/ourfacilities/kelvinhydrodynamicslaboratory/, 2025, 24th February 2025.

Collins, I., Hossain, M., Dettmer, W., Masters, I., 2021. Flexible membrane structures for wave energy harvesting: a review of the developments, materials and computational modelling approaches. Renew. Sustain. Energy Rev. 151, 111478.

Falcão, A.F.D.O., 2010. Wave energy utilization: a review of the technologies. Renew. Sustain. Energy Rev. 14 (3), 899–918.

Farley, F.J.M., Rainey, R.C.T., 2011. U.S. Patent No. 7,980,071. U.S. Patent and Trademark Office, Washington, DC.

Farley, F.J.M., Rainey, R.C.T., Chaplin, J.R., 2012. Rubber tubes in the sea. Philos. Trans. R. Soc. A Math. Phys. Eng. Sci. 370 (1959), 381–402.

Guo, B., Ringwood, J.V., 2021. A review of wave energy technology from a research and commercial perspective. IET Renew. Power Gener. 15 (14), 3065–3090.

Heller, V., Chaplin, J.R., Farley, F.J.M., Hann, M.R., Hearn, G.E., 2010. Physical model tests of the anaconda wave energy converter. In: Proc. 1st IAHR European Congress.

Huang, Y., Xiao, Q., Alarcon, G.I., Yang, L., Dai, D., Abad, F., et al., 2023. A CFD-FEM analysis for anaconda WEC with mooring lines. In: Proceedings of the 15th European Wave and Tidal Energy Conference 2023, p. 163.

Huang, Y., Xiao, Q., Idarraga, G., Yang, L., Dai, S., Abad, F., Brennan, F., Lotfian, S., 2025. Bio-inspired adaptive flexible tube wave energy converters: resonant fluid-structure interaction and power extraction. Phys. Fluids 37 (5). https://doi.org/10.1063/5.0270834.

Jean, P., Wattez, A., Ardoise, G., Melis, C., Van Kessel, R., Fourmon, A., et al., 2012. Standing wave tube electro active polymer wave energy converter. Electroactive Polymer Actuators and Devices (EAPAD) 2012 8340, 75–95. SPIE.

Kelvin hydrodynamics laboratory. https://www.checkmateflex.com/, 2025, 8th March 2025.

Lighthill, J., 1978. Waves in Fluids. cambridge univ[J]. P ress, Cambridge.

Mendes, A.C., Paredes, L.M.A., Gil, F.A.S., Chaplin, J.R., 2014. Small-scale model tests of a rubber-tube wave energy converter with pneumatic power take-off. Int. Conf. Offshore Mech. Arctic Eng. 45530, V09AT09A029. American Society of Mechanical Engineers.

Mendes, A.C., Braga, F.P., Paredes, L.M.A., Chaplin, J.R., 2017. Performance assessment of the ANACONDA WEC in regular waves at 1: 50 model scale. Int. Conf. Offshore Mech. Arctic Eng. 57786, V010T09A016. American Society of Mechanical Engineers.

Mohapatra, S.C., Soares, C.G., 2024. Oblique wave interaction with an integrated wave energy extraction system. In: Innovations in Renewable Energies Offshore. CRC Press, pp. 835–843.

Mohapatra, S.C., Amouzadrad, P., Bispo, I.B.D.S., Guedes Soares, C., 2025. Hydrodynamic response to current and wind on a large floating interconnected structure. J. Mar. Sci. Eng. 13 (1), 63.

Moretti, G., Herran, M.S., Forehand, D., Alves, M., Jeffrey, H., Vertechy, R., Fontana, M., 2020. Advances in the development of dielectric elastomer generators for wave energy conversion. Renew. Sustain. Energy Rev. 117, 109430.

Mwasilu, F., Jung, J.W., 2019. Potential for power generation from ocean wave renewable energy source: a comprehensive review on state-of-the-art technology and future prospects. IET Renew. Power Gener. 13 (3), 363–375.

Ning, D.Z., Wang, R.Q., Chen, L.F., Sun, K., 2019. Experimental investigation of a land-based dual-chamber OWC wave energy converter. Renew. Sustain. Energy Rev. 105, 48–60.

Orphin, J., Schmitt, P., Nader, J.R., Penesis, I., 2022. Experimental investigation into laboratory effects of an OWC wave energy converter. Renew. Energy 186, 250–263.

Pedley, T.J., 1980. The Fluid Mechanics of Large Blood Vessels (No Title).

Uihlein, A., Magagna, D., 2016. Wave and tidal current energy–A review of the current state of research beyond technology. Renew. Sustain. Energy Rev. 58, 1070–1081.

Yu, H., Bai, Z., Shi, Y., Zhao, C., Liu, X., Wang, Y., 2024. Hydrodynamic performance of an elastic capsule oscillating water column type WEC: an experimental study. Appl. Ocean Res. 142, 103850.